

Research Article

Microcavity Silicon Photodetectors at 1.55 μm

M. Casalino,¹ G. Coppola,¹ M. Giofrè,¹ M. Iodice,¹ L. Moretti,² I. Rendina,¹ and L. Sirleto¹

¹ Department of Naples, Institute for Microelectronics and Microsystems, National Council of Research, Via P. Castellino 111, 80131 Naples, Italy

² Department of Mathematics, Seconda Università degli Studi di Napoli, Via Vivaldi 43, 81100 Caserta, Italy

Correspondence should be addressed to M. Casalino, maurizio.casalino@na.imm.cnr.it

Received 25 June 2010; Revised 16 September 2010; Accepted 22 October 2010

Academic Editor: Snjezana Tomljenovic-Hanic

Copyright © 2011 M. Casalino et al. This is an open access article distributed under the Creative Commons Attribution License, which permits unrestricted use, distribution, and reproduction in any medium, provided the original work is properly cited.

The design, the realization, and the characterization of silicon resonant cavity enhanced (RCE) photodetectors, working at 1.55 μm , are reported. The photodetectors are constituted by a Fabry-Perot microcavity incorporating a Schottky diode. The working principle is based on the internal photoemission effect. We investigated two types of structures: top and back-illuminated. Concerning the top-illuminated photodetectors, a theoretical and numerical analysis has been provided and the device quantum efficiency has been calculated. Moreover, a comparison among three different photodetectors, having as Schottky metal: gold, silver, or copper, was proposed. Concerning the back-illuminated devices, two kinds of Cu/p-Si RCE photodetectors, having various bottom-mirror reflectivities, were realized and characterized. Device performances in terms of responsivity, free spectral range, and finesse were theoretically and experimentally calculated in order to prove an enhancement in efficiency due to the cavity effect. The back-illuminated device fabrication process is completely compatible with the standard silicon technology.

1. Introduction

In the last two decades, there has been growing interest in photonic devices based on Si-compatible materials [1, 2] in the field of both optical telecommunications and optical interconnects. In this context, tremendous progresses in the technological processes have allowed to realize effectively fully CMOS compatible optical components, such as low-loss waveguides, high-Q resonators, high speed modulators, couplers, and optically pumped lasers [3–8]. All these devices have been developed to operate in the wavelength range from the C optical band (1528–1561 nm) to the L optical band (1561–1620 nm) where the defect-free intrinsic bulk Si has minimal absorption. On the other hands, this transparency window limits the Si applications as absorbing material for infrared photodetection, so that the development of high-performance waveguide-integrated photodetectors on Si-CMOS platform has remained an imperative but unaccomplished task. In order to develop all Si photodetectors and to take advantage of the low-cost standard Si-CMOS processing technology without additional materials or process steps, a number of options have been proposed, in particular, the two-photon absorption (TPA) [9], the incorporation of

optical dopants/defects with mid-bandgap energy levels into the Si lattice [10, 11], and the internal photoemission effect (IPE) [12]. The IPE has been recently used also in silicon photodetectors realized with plasmonics structures [13, 14].

Silicon infrared photodiodes based on the IPE are usually employed in infrared imaging systems [15]. Unfortunately, due to their low potential barriers (≤ 0.25 eV), they must work at cryogenic temperature (70 K) in order to avoid high dark-current densities. The main advantages of these devices reside in their large bandwidth and simple fabrication process, but, due to the leakage photon flux within the metallic layer, their quantum efficiency (number of collected electrons per incident photon) is very small. In this paper, with the aim to enhance the device quantum efficiency at room temperature, top- and back-illuminated photodetectors at 1.55 μm , based on IPE and incorporated into a microcavity structure, have been investigated. A theoretical and numerical analysis of a top-illuminated structure has been provided, and in order to estimate the device theoretical quantum efficiency, we have taken advantage of the analytical formulation of the Fowler's theory [16], including the image force effect and its extension for thin films. On the other

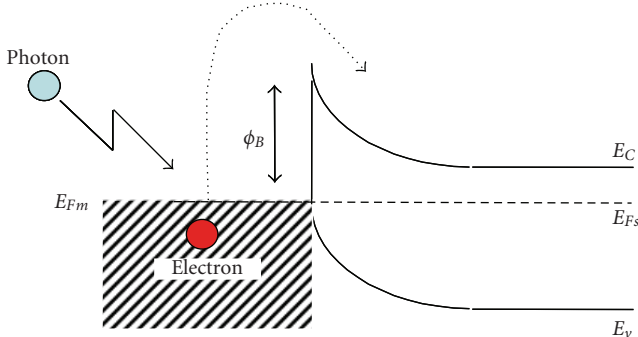


FIGURE 1: Energy band diagram for a metal-semiconductor junction.

hand, concerning the device optical analysis, a numerical approach, based on the transfer matrix method (TMM), has been implemented. We prove that a significant enhancement in quantum efficiency can be achieved by using an RCE structure. A comparison among three different Schottky barrier silicon photodetectors, having as metal layers: gold, silver, and copper, has been proposed. Our numerical results prove that in order to improve the device quantum efficiency, the Schottky barrier plays a key role.

However, concerning the top-illuminated structure, the crucial point is the realization of a metal thin film (semitransparent). The precise control of the thin metal

thickness and an acceptably low defect concentration are not trivial tasks. Therefore, the design, the realization, and the characterization of back-illuminated RCE photodetectors having a thick metal layer as top mirror, have been reported. In order to experimentally prove the responsivity (ratio between photogenerated current and incident optical power) enhancement, which can be achieved by using a resonant structure, a comparison between a Schottky diode, with and without Bragg reflector, has been made. An improvement in responsivity at $1.55 \mu\text{m}$ has been theoretically and experimentally demonstrated for the Cu/p-Si Schottky diode provided by a high reflectivity Bragg mirror.

2. Internal Photoemission Theory

Internal photoemission is the optical excitation of electrons in the metal to an energy above the Schottky barrier and then transport of these electrons to the conduction band of the semiconductor (Figure 1).

The standard theory of the photoemission from a metal into the vacuum is due to Fowler [16]. In a gas of electrons obeying the Fermi-Dirac statistics, if the energy of the incoming photons is close to the potential barrier ($h\nu \approx \Phi_B$), the fraction (F_e) of the absorbed photons, which produce photoelectrons with the appropriate energy and moment before scattering to contribute to the photocurrent, is given by

$$F_e = \frac{\left[(h\nu - (\phi_{B0} - \Delta\phi_B))^2 + \left(\frac{kT\pi^2}{3} \right) - 2(kT)^2 e^{-h\nu - ((\phi_{B0} - \Delta\phi_B))/kT} \right]}{8kTE_F \log[1 + e^{(h\nu - (\phi_{B0} - \Delta\phi_B))/kT}]}, \quad (1)$$

where $h\nu$ is photon's energy, Φ_{B0} is the potential barrier at zero bias, $\Delta\phi_B$ is the lowering due to the image force effect (as we will see later), and E_F is the metal Fermi level. As it is possible to see in (1), F_e is strongly depending on the potential barrier height of the metal-semiconductor interface.

In order to study the quantum efficiency for thin metal films, the theory must be further extended, taking into account multiple reflections of the excited electrons from the surface of the metals film, in addition to the collisions with phonons, imperfections, and cold electrons. Assuming a thin metal film, a phenomenological, semiclassical, ballistic transport model for the effects of the scattering mechanisms resulting in a multiplicative factor for quantum efficiency was developed by Vickers [17]. According to this model, the accumulated probability P_E that the electrons will have sufficient normal kinetic energy to overcome the potential barrier is given by

$$P_E \cong \left[1 - e^{-(d/L_e)} \right]^{1/2}, \quad (2)$$

where d is the metal thickness and L_e is the mean free path.

In order to complete the internal photoemission theory, the image force between an electron and the metal surface must be taken into account. The image force effect causes a lowering ($\Delta\phi_B$) and displacement (x_m) of the metal-semiconductor interface potential barrier. These barrier lowering and displacement are given by [18]

$$x_m = \sqrt{\frac{q}{16\pi\epsilon_{Si}} \frac{W}{|V_{Bias}|}}, \quad \Delta\phi_B = \sqrt{\frac{q}{4\pi\epsilon_{Si}} \frac{|V_{Bias}|}{W}}, \quad (3)$$

where ϵ_{Si} is the permittivity of silicon (10^{-12} C/cmV), W is the depletion width, and V_{Bias} the applied bias voltage.

Finally, the probability that an electron travels from the metal-semiconductor interface to the Schottky barrier maximum without scattering in the Si is taken into account by the barrier collection efficiency η_c , which is given by [19]

$$\eta_c = e^{-(x_m/L_s)}, \quad (4)$$

where L_s is the electron scattering length in the silicon. It is worth noting that by increasing the bias voltage, a shift of Schottky barrier closer to metal-semiconductor interface is obtained. Therefore, the barrier collection efficiency increases.

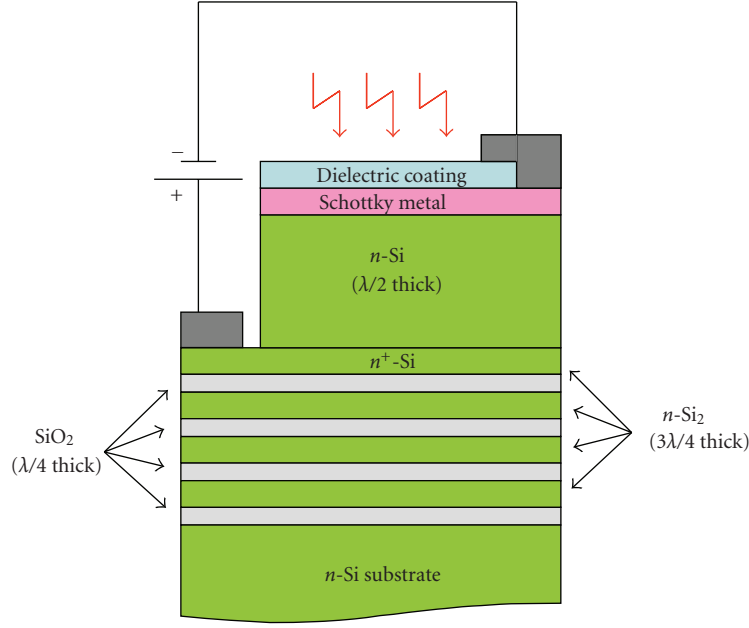


FIGURE 2: Schematic cross-section of top-illuminated RCE Schottky photodetector.

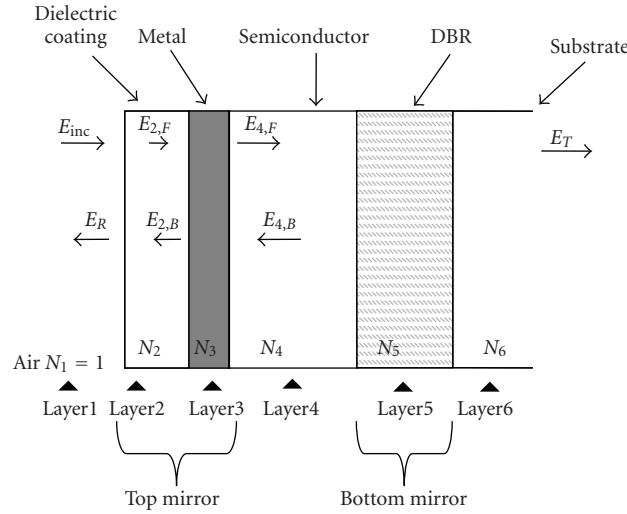


FIGURE 3: Schematic of the multilayer RCE photodetector.

3. Top-Illuminated Device

3.1. Proposed Device. The sketch of the proposed top-illuminated photodetector is shown in Figure 2.

The resonant cavity is a Fabry-Perot surface normal structure. It is formed by a buried reflector, a metallic top mirror, and, in the middle, a $\lambda/2$ silicon cavity. On top of the $\lambda/2$ silicon cavity has been deposited a semitransparent Schottky metal and a coating dielectric layer, working as top reflector of the resonant cavity. We point out that our structure is different from the RCE Schottky photodetectors in which the Schottky contact is only an electric contact and not the active layer. In our device, the metal layer works as

top contact, as active (absorbing) layer, and as mirror. This is the crucial point and the novelty of our device.

The distributed Bragg reflector (DBR) could be formed by alternate layers of Si and SiO₂ having refractive indices 3.45 and 1.45, respectively. One of the many benefits of this reflector is the large index contrast provided by Si/SiO₂ structures allowing the realization of high-reflectivity and wide spectral stop-band DBR. Commercially reproducible dielectric mirrors consisting of a two-period DBR fabricated using a double silicon-on-insulator (DSOI) process have been successfully realized showing a reflectivity of 92.7% at 1550 nm [20, 21]. In the same way, it could be possible to realize DBR formed of more than two Si/SiO₂ pairs. The

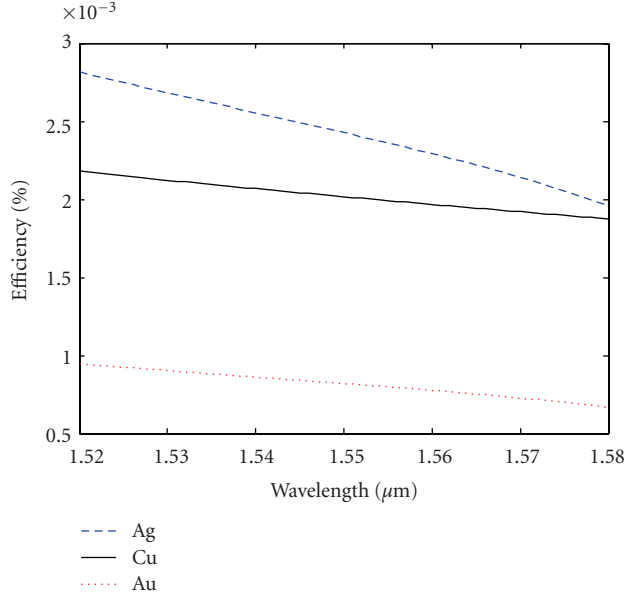


FIGURE 4: Calculated quantum efficiency versus wavelength for devices without DBRs having various metals as top mirror: Ag (blue dashed line), Cu (black solid line), and Au (red dotted line).

TABLE 1: Optical and electrical properties for three metals: gold, silver, and copper.

Metal	Complex refractive index (N)	Mean free path (L_e) [μm]	Fermi level (E_F) [eV]	Potential barrier (Φ_B) [eV]
Au	0.174-j9.960	0.055	5.530	0.780
Ag	0.450-j9.290	0.057	5.480	0.780
Cu	0.145-j9.830	0.045	7.050	0.580

use of SOI substrate has been investigated extensively for the fabrication of Si-based photodetectors; this technique is particularly attractive given the widespread acceptance of SOI technology as a platform for high performance CMOS [22]. The benefits gained by using SOI substrates, due to the high index contrast of the buried oxide, would be the same offered by substrates constituted with more Si/SiO₂ pairs. Starting from these considerations, in our design we propose a DBR centred at 1.55 μm formed by 4 periods of Si/SiO₂ having thicknesses of 340 nm (limitations in fabrication process usually do not allow to realize a Si layer thickness as thin as $(\lambda/4n)$; for this reason a thickness of $(3\lambda/4n)$ was considered [20]) and 270 nm, respectively. Reflectivity of the proposed Si/SiO₂ DBR is 0.99 at 1550 nm.

In order to achieve an Ohmic contact, the top layer of the DBR is supposed to be realized by a very thin but heavily doped 10^{19} cm^{-3} silicon layer. Concerning the top reflector of the resonant cavity, we consider three metals: gold, silver, and copper, whose optical and electrical properties are summarized in Table 1 [21, 23, 24].

The efficiency of the RCE-PD is given by (5) [17]

$$\eta = A_T F_e P_E \eta_c, \quad (5)$$

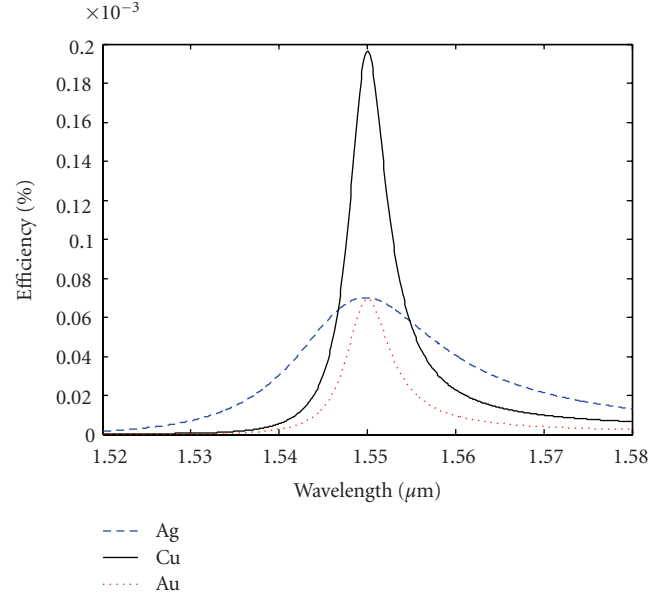


FIGURE 5: Calculated quantum efficiency versus wavelength for devices with DBRs formed by 4 Si/SiO₂. Top mirror is realized with various metals: Ag (blue dashed line), Cu (black solid line), and Au (red dotted line).

where A_T is the total optical absorbance of the metal while F_e , P_E , and η_c have been previously introduced. The cavity effect is taken into account in the calculation of the A_T factor, which has been carried out by using a transfer matrix method (TMM) [24, 25].

3.2. Absorbance Calculation and Quantum Efficiency. In order to estimate the quantum efficiency, the calculation of the absorbance (A_T) is numerically carried out by TMM. Normal incidence condition and the restriction to variations of $n(z)$, that is, the unidimensional refractive index profile, along the propagation direction (z) are taken into account.

Let us consider a general structure for proposed photodetector in which layer 3 is the absorbing material (Figure 3).

As shown in Figure 3, let $E_{2,F}$ ($E_{4,F}$) and $E_{2,B}$ ($E_{4,B}$) be the frequency domain electric field complex amplitudes of the forward and backward travelling plane waves in layer 2 (layer 4); the total powers incident on and going out from the metal are

$$\begin{aligned} P_{\text{input}} &= \frac{n_2}{2\eta_0} |E_{2,F}|^2 + \frac{n_4}{2\eta_0} |E_{4,B}|^2 \\ &= \left(n_2 \left| \frac{M_{A11}}{M_{TOT11}} \right|^2 + n_4 \left| \frac{M_{B21}}{M_{TOT11}} \right|^2 \right) \frac{|E_{\text{inc}}|^2}{2\eta_0}, \\ P_{\text{output}} &= \frac{n_2}{2\eta_0} |E_{2,B}|^2 + \frac{n_4}{2\eta_0} |E_{4,F}|^2 \\ &= \left(n_2 \left| \frac{M_{A21}}{M_{TOT11}} \right|^2 + n_4 \left| \frac{M_{B11}}{M_{TOT11}} \right|^2 \right) \frac{|E_{\text{inc}}|^2}{2\eta_0}, \end{aligned} \quad (6)$$

where η_0 is the vacuum characteristic impedance.

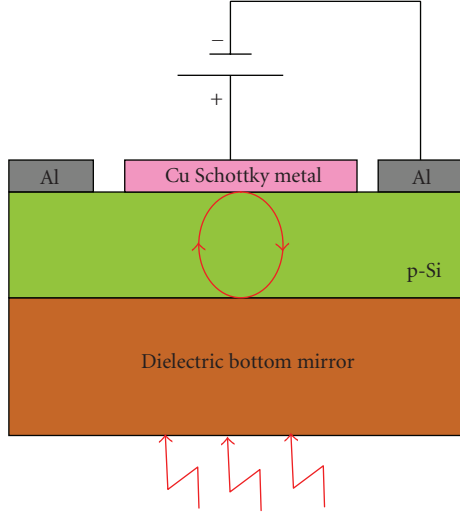


FIGURE 6: Schematic cross-section of the proposed back-illuminated RCE Schottky photodetector.

Air being the first layer considered ($n_1 = 1$) and P_{inc} being the power incident on the whole system, absorbance in the metal layer is given by

$$A_T = \frac{P_{input} - P_{output}}{P_{inc}} = \left\{ \left(n_2 \left| \frac{M_{A_{11}}}{M_{TOT_{11}}} \right|^2 + n_4 \left| \frac{M_{B_{21}}}{M_{TOT_{11}}} \right|^2 \right) - \left(n_2 \left| \frac{M_{A_{21}}}{M_{TOT_{11}}} \right|^2 + n_4 \left| \frac{M_{B_{11}}}{M_{TOT_{11}}} \right|^2 \right) \right\} \quad (7)$$

where n_2 and n_4 are the real parts of the refractive index of the 2th and 4th layer, respectively.

We point out that we could apply the power balance to the whole device instead that to the only metal layer, but, in this case, we would have considered also the absorbance contribution due to the layer heavily doped on top of the DBR necessary to achieve Ohmic contact (Figure 2).

A_T depends critically upon the metal thickness. The value of thickness must be a compromise between the top reflectivity value and the absorbance of metal layer. In order to calculate the maximum absorbance, the resonance condition must be imposed

$$2\beta(\lambda_0)L + \psi_1(\lambda_0) + \psi_2(\lambda_0) = 2\pi, \quad (8)$$

where $\beta = 2n\pi/\lambda_0$ is the propagation constant, L is the thickness of silicon cavity and, ψ_1 and ψ_2 are the phases introduced by the top and bottom mirror, respectively.

An analytical formulation of the quantum efficiency for a simplified RCE-PD structure with lossless mirrors was given by Kishino et al. [26]. In the case of an absorbing mirror, such as the semitransparent metallic top mirror of RCE Schottky PDs, the previous formulation is no longer valid. Therefore, in order to calculate the device maximum

TABLE 2: Cavity parameter coming out from our simulations.

Metal	Cavity thick-ness (L) [μm]	thick-ness (d) [nm]	R_1	Ψ_1 [rad]	A_T	Q value
Au	0.420	30	0.920	-2.140	0.780	525
Ag	0.410	20	0.730	-2.110	0.930	153
Cu	0.420	32	0.930	-2.360	0.740	585

quantum efficiency, the following methodology has been adopted:

- (1) bottom-mirror reflectivity and phase (R_2 , ψ_2) have been calculated. They result in 0.990 and 3.11 rad, respectively,
- (2) top-mirror reflectivities and phases (R_1 , ψ_1) have been calculated for metal thicknesses ranging from 0 to 50 nm consequently, the value of silicon cavity thickness yielding a resonance condition can be obtained by (8). Finally, the resulting absorbance is calculated using (7). We obtain a curve of absorbance depending on the metal thickness in the range of 0–50 nm and we consider the maximum,
- (3) dielectric coating thickness, chosen in order to avoid perturbation of resonance condition, is a Si_3N_4 layer, having refractive index 2.0 and thickness of 390 nm, and
- (4) at this point, the parameters of the optimized cavity are fixed and the quantum efficiency as a function of wavelength in the range of interest can be calculated using (1)–(5), (7).

The parameters calculated by the aforementioned methodology have been summarized in Table 2.

Efficiency versus wavelength for various metals has been reported for a device without DBR in Figure 4 and with DBR in Figure 5, respectively.

It is worth noting that a significant quantum efficiency enhancement of two order of magnitude is achieved by using a resonant cavity structure. We note that the copper top contact cavity has the best quantum efficiency (about 0.2%, corresponding to a responsivity of 2.5 mA/W at 1550 nm) and selectivity due to its lower potential barrier and to its higher reflectivity, respectively. It is interesting in comparing gold and silver, due to the same value of barrier (Table 1), we get the same order of efficiency (about 0.06%, corresponding to a responsivity of 0.75 mA/W at 1550 nm), but in the case of gold a better selectivity, due to the higher reflectivity, is obtained.

4. Back-Illuminated Device

4.1. Proposed Device. The sketch of the proposed back-illuminated device is shown in Figure 6.

The resonant cavity is a surface normal Fabry-Perot structure. It is formed by a dielectric bottom mirror, a metallic top mirror, and, in the middle, a silicon cavity. The advantage of a back-illuminated device is that the top

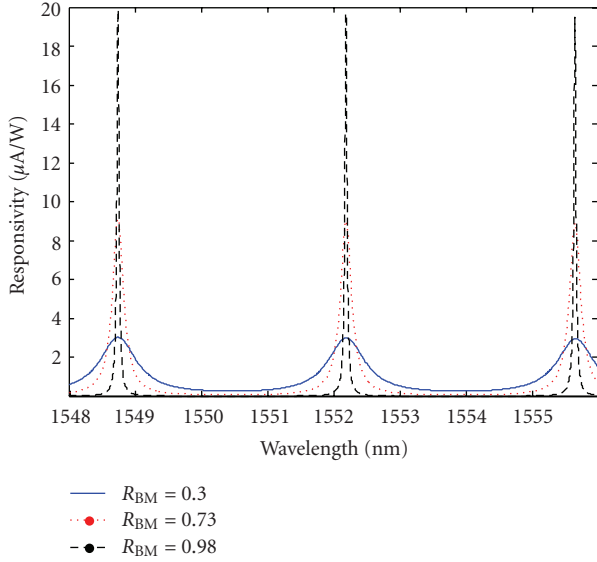


FIGURE 7: Responsivity versus Wavelength at bottom-mirror reflectivities (R_{BM}) of 0.3 (blue solid line), 0.73 (red dotted line), and 0.98 (black dashed line).

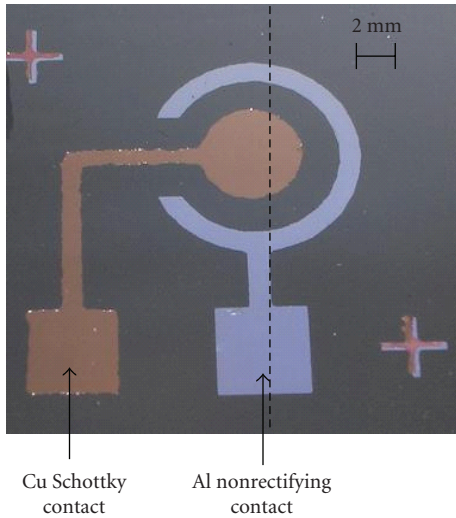


FIGURE 8: Top view of the back-illuminated realized photodetector.

mirror can be realized very thick reducing the importance of the roughness control during metal deposition process. The dielectric bottom reflector will be realized by alternating layers of amorphous hydrogenated silicon (a-Si:H) and silicon nitride (Si_3N_4) having $\lambda/4$ thicknesses.

4.2. Responsivity Calculation. By (1)–(5) and (7), devices having bottom-mirror reflectivities (R_{BM}) of 0.3 (reflectivity of a silicon/air interface), 0.73, and 0.98 were numerically investigated. All optical and electrical properties for silicon and copper used in our simulations are reported in Table 3 [21, 23–27].

TABLE 3: Optical and electrical properties for silicon and copper used in our simulations.

	Complex refractive index at 1550 nm	Thickness [μm]	Mean free path (L_e) [μm]	Fermi level (E_F) [eV]	Potential barrier (Φ_B) [eV]
Copper (Cu)	0.145-j9.830	0.20	0.045	7.050	0.720
Silicon	3.48	100	—	—	—

TABLE 4: Cavity parameters coming out from our simulations.

	Peak responsivity [$\mu\text{A/W}$]	Cavity finesse
Cu/p-Si photodiode with bottom reflectivity at 1550 nm of 0.30	3	4.7
Cu/p-Si photodiode with bottom reflectivity at 1550 nm of 0.73	9.1	16.5
Cu/p-Si photodiode with bottom reflectivity at 1550 nm of 0.98	19.9	89

In Figure 7, responsivity (linked to the efficiency by the formula: $R = (\lambda[\text{nm}]/1242)\eta$) versus wavelength at various bottom-mirror reflectivities is reported.

The results coming out of our simulation are summarized in Table 4.

In all cases, the free spectral range is 3.3 nm. It is worth noting that a responsivity enhancement is achieved by using resonant cavity structure at higher finesse. The maximum responsivity of $19.9 \mu\text{A/W}$ obtained in our simulations is about two orders of magnitude lower compared with the top-illuminated structure numerically investigated above. This is expected from the fact that in top illuminated structure the goal was to optimize the device in order to get the highest efficiency while in this back-illuminated structure the layer thicknesses are chosen taking into account our capability to realize a preliminary device in order to make a comparison between theoretical and experimental data.

4.3. Device Fabrication. In order to validate our numerical results, we only fabricated back-illuminated structures in two variants: one with high-reflectivity bottom mirror realized with 5 pairs of a-Si:H/ Si_3N_4 and one with a low reflectivity bottom mirror realized with simple silicon/air interface. Both structures have been provided by Cu metal working as the top mirror.

The samples were fabricated starting from a slightly doped (10^{14} cm^{-3}) p-type bi-polished $100\text{-}\mu\text{m}$ -thick silicon wafer.

The collecting ohmic contact was realized on the top of the samples. The collecting contact was made by a 200-nm -thick aluminum film, thermally evaporated at $3 \cdot 10^{-6}$ mbar and 150°C , and patterned by a lift-off process of photoresist Shipley S1813 which, deposited by a spincoater at 4000 rpm, has a thickness of $1.4 \mu\text{m}$. Then, an annealing at 475°C in

TABLE 5: Value of thicknesses and refractive indices as calculated.

	\overline{D} [nm]	n_{1550}
a-Si:H	108	3.58
Si ₃ N ₄	220	1.82

nitrogen for 30 min, in order to get a not-rectifying behavior, was carried out [28].

On the back of one device, a multilayer Bragg mirror was fabricated by Plasma Enhanced Chemical Vapor Deposition technique (PECVD). The mirror is composed by a quarter-wave stack of a-Si:H and Si₃N₄ layers, having nominal refractive index, at 1550 nm, of 3.52 and 1.82, respectively. Silicon nitride was deposited at pressure of 1.2 mbar, temperature of 250°C, at 30 W of RF power. In the deposition chamber, 10 sccm of NH₃, 88 sccm of SiH₄ (5% in He), and 632 sccm of N₂ were flowed. The deposition rate is 22.93 nm/min, and the suitable Si₃N₄ thickness was obtained with a process time of 9 min and 17 sec. The amorphous hydrogenated silicon, instead, was deposited at pressure of 0.8 mbar, temperature of 250°C, power of 2 W, and a SiH₄ (5% in He) flow of 600 sccm. The a-Si:H deposition rate is 3.15 nm/min, and the suitable thickness was obtained with a process time of 34 min and 56 sec.

Finally, the Schottky contact was fabricated on top of both samples. Copper was thermally evaporated and patterned by liftoff, so obtaining a metal thickness of 200 nm, thicker than optical field penetration depth. The collecting contact and the Schottky contact are shaped by a ring and a disk having radius of about 2 mm, as shown in Figure 8.

4.4. Device Characterization

4.4.1. Bragg Mirror Reflectivity Characterization. As far as the realization of our device is concerned, the crucial point is the Bragg mirror. Bragg reflectivity measurements were carried out by means of Spectroscopic Ellipsometry (SE) [29, 30]. Spectroscopic ellipsometric data were acquired by a Jobin Yvon UVISSEL-NIR phase-modulated spectroscopic ellipsometer apparatus, at 70° angle of incidence, operating from 280 to 1600 nm. The optical properties of a-Si:H and Si₃N₄, that is, the complex refractive index dispersion spectra, were calculated using the Tauc-Lorentz dispersion model [31–33]. The thicknesses and the refractive indices at $\lambda = 1550$ nm, for both a-Si:H and Si₃N₄ films, are summarized in Table 5.

The Bragg mirror theoretical model is composed by five distinct pairs of a-Si:H/Si₃N₄ layers, deposited on single-crystal silicon substrate, and by a superficial roughness, modelled by a Bruggeman effective medium approximation (EMA) [34], and consisting of 50% of air and 50% of a-Si. The fitting procedure between the experimental data and the theoretical model was executed using the Levenberg-Marquardt algorithm and returned a fit goodness factor $\chi^2 = 2.9$. Starting from the results shown in Table 5, a simulated reflectivity at normal incidence has been reported in Figure 9 (solid line).

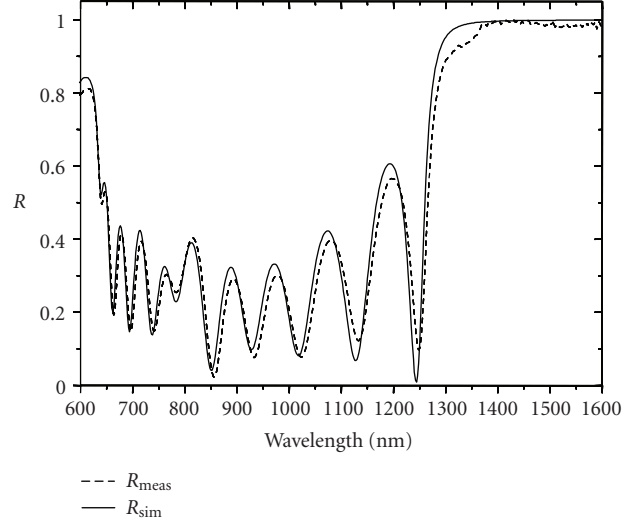


FIGURE 9: Measured and simulated reflectivity of the Bragg mirror, formed by 5 pairs of a-Si:H/Si₃N₄, from 600 to 1600 nm at normal incidence.

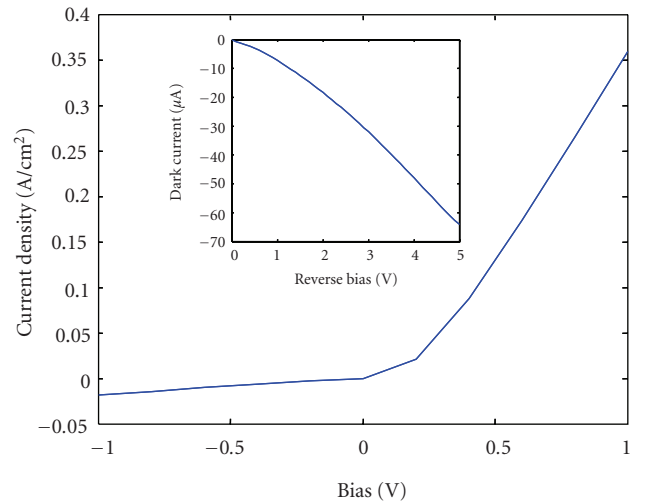


FIGURE 10: J-V characteristic of the realized Cu/p-Si Schottky diode. The inset shows diodes dark current.

Finally, the reflectivity spectra of the Bragg reflector was measured at normal incidence by means of a Y optical reflection probe (Avantes), connected to a white light source and to an optical spectrum analyzer (Ando, AQ6315B). The comparison between simulated and measured (dotted line) Bragg mirror reflectivity, for light normally incident in the range 600–1600 nm, is reported in Figure 9.

4.4.2. Electrical Characterization. Typical density current-voltage (J-V) curve of Cu/p-Si diode, obtained by a parameter analyzer (Hewlett Packard 4145B), is depicted in Figure 10.

The Schottky barrier height (SBH) was deduced fitting the experimental J-V characteristic, in the forward bias

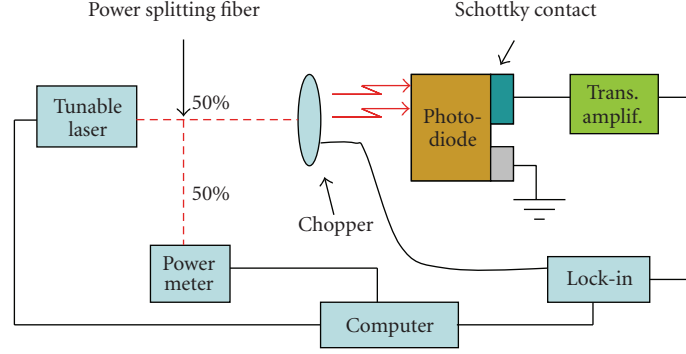
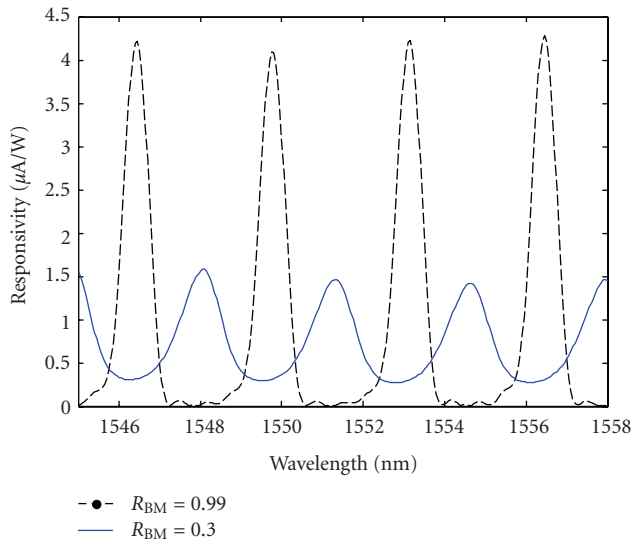


FIGURE 11: Experimental setup for external responsivity measurements.

FIGURE 12: Measured responsivity versus wavelength for two realized devices: having bottom mirror reflectivity (R_{BM}) of 0.3 (blue solid line) and 0.99 (black dashed line), respectively.

region, to the following equation of the Schottky diode (9) [18]:

$$J = A^{**} T^2 e^{-\Phi_B/V_T} \left(e^{-((V - R_s I)/\eta V_T)} - 1 \right), \quad (9)$$

where R_s is the series resistance, Φ_B the potential barrier, η the ideality factor, T the absolute temperature, and V_T is the thermal voltage. The calculated SBH is 0.72 ± 0.01 eV.

The maximum detectable wavelength is given by (10):

$$\lambda_{\max} [\text{nm}] = \frac{1242}{\phi_B}. \quad (10)$$

We obtain that Cu/p-Si photodiodes are able to detect wavelengths up to 1725 nm.

4.4.3. Optical Characterization. The experimental set-up for external responsivity measurements is shown in Figure 11. The laser beam emitted by a wavelength tunable laser is split by a Y fiber junction. One branch is used to monitor the

optical power, while the other one is collimated, chopped, and sent onto the device. The photocurrent produced by our device is measured by a lock-in amplifier. A transimpedance amplifier is employed to provide a reverse bias to the photodetector and at the same time for reducing the dark current. The dark current cancellation circuit realised by using a transimpedance amplifier has a limited bandwidth; however, it is adequate for our scope, that is dc or quasistatic measurements [35].

Responsivity measurements were carried out in the range of 1545–1558 nm (step of 0.05 nm). Figure 12 shows the room temperature responsivity versus the wavelength in two conditions: device with a bottom-mirror reflectivity (R_{BM}) of 0.3 (blue solid line) and 0.99 (black dashed line), respectively. The measured free spectral range of 3.3 nm agrees with the value numerically calculated. By looking at device having $R_{BM} = 0.3$, the measured cavity finesse F and responsivity are 2.9 and $1.6 \mu\text{A/W}$, respectively. Moving our attention to the device having $R_{BM} = 0.99$, we get a measured cavity finesse F and responsivity of 4.7 and $4.3 \mu\text{A/W}$, respectively.

By comparing Figures 7 and 12, we note that while the experimental and numerical free spectral range agree, as far as finesse and peak responsivity are concerned, experimental and numerical values show a discrepancy. In our opinion, such a discrepancy can be due to the cavity losses, which are not taken into account in our simulations. In fact, it is well known that if we assume a Fabry-Perot interferometer having ideal plane-parallel plates, the finesse is determined only by the reflectivity R of the mirrors. In practice, however, deviations of the surfaces from an ideal plane, slight inclinations of the two surfaces, and surface irregularities cause imperfect superposition of the interfering waves. This results in a broadening of the transmission peak and a decreasing of the total finesse [36].

5. Conclusions

In this paper, a new approach for sub-bandgap detection at $1.55 \mu\text{m}$ in Si-based devices is investigated. The proposed devices are RCE structures incorporating silicon photodetectors based on the internal photoemission effect. We investigated two types of structures: top and back illuminated.

Concerning the top-illuminated photodetectors, a device theoretical investigation has been carried out. A methodology based on TMM has been implemented in order to design and to optimize the structures. We proved that a significant enhancement in quantum efficiency, of about two orders of magnitude, can be achieved due to the effect of the Fabry-Perot microcavity. Moreover, a comparison among three different photodetectors, having as Schottky metal: gold, silver, or copper, was proposed. We proved that due to its lowest potential barrier, the best quantum efficiency has been obtained by considering copper as Schottky metal, demonstrating that the metal-silicon interface potential barrier plays a key role.

It is worthy noting that the fabrication of top illuminated devices could be not simple, in fact, the precise control of the thin metal thickness and an acceptably low defect concentrations are not trivial tasks. For these reasons, back illuminated devices constituted by a thick metal layer as top mirror have been realized.

Concerning the back-illuminated photodetectors, a theoretical and experimental investigation on devices having bottom mirror reflectivities of 0.3 and 0.99, respectively, have been carried out. Simulated and measured responsivities around 1550 nm show a good agreement from a qualitative point of view, demonstrating that the responsivity enhancement is strictly linked to the increased cavity finesse.

Even if the measured responsivities could be already suitable for power monitoring applications, we believe that our results could be further improved by investigating more complex microcavities at higher finesse (for example, ring resonator), which could be also very promising in the integration of photonic components with integrated circuit electronics enabling interconnection bandwidth that is not limited by the RC time constant and reliability constraints of metal lines.

References

- [1] L. C. Kimerling, L. Dal Negro, S. Saini et al., "Monolithic silicon microphotronics," in *Silicon Photonics*, L. Pavesi and D. J. Lockwood, Eds., vol. 94 of *Topics in Applied Physics*, pp. 89–119, Springer, Berlin, Germany, 2004.
- [2] B. Jalali and S. Fathpour, "Silicon photonics," *Journal of Lightwave Technology*, vol. 24, no. 12, pp. 4600–4615, 2006.
- [3] L. K. Rowe, M. Elsey, N. G. Tarr, A. P. Knights, and E. Post, "CMOS-compatible optical rib waveguides defined by local oxidation of silicon," *Electronics Letters*, vol. 43, no. 7, pp. 392–393, 2007.
- [4] L. Vivien, D. Pascal, S. Lardenois et al., "Light injection in SOI microwaveguides using high-efficiency grating couplers," *Journal of Lightwave Technology*, vol. 24, no. 10, pp. 3810–3815, 2006.
- [5] Q. Xu, S. Manipatruni, B. Schmidt, J. Shakya, and M. Lipson, "12.5 Gbit/s carrier-injection-based silicon micro-ring silicon modulators," *Optics Express*, vol. 15, no. 2, pp. 430–436, 2007.
- [6] C. P. Michael, M. Borselli, T. J. Johnson, C. Chrystal, and O. Painter, "An optical fiber-taper probe for wafer-scale microphotonic device characterization," *Optics Express*, vol. 15, no. 8, pp. 4745–4752, 2007.
- [7] A. Liu, L. Liao, D. Rubin et al., "High-speed optical modulation based on carrier depletion in a silicon waveguide," *Optics Express*, vol. 15, no. 2, pp. 660–668, 2007.
- [8] A. Liu, H. Rong, R. Jones, O. Cohen, D. Hak, and M. Paniccia, "Optical amplification and lasing by stimulated Raman scattering in silicon waveguides," *Journal of Lightwave Technology*, vol. 24, no. 3, pp. 1440–1455, 2006.
- [9] T. K. Liang, H. K. Tsang, I. E. Day, J. Drake, A. P. Knights, and M. Asghari, "Silicon waveguide two-photon absorption detector at 1.5 μm wavelength for autocorrelation measurements," *Applied Physics Letters*, vol. 81, no. 7, p. 1323, 2002.
- [10] J. D. B. Bradley, P. E. Jessop, and A. P. Knights, "Silicon waveguide-integrated optical power monitor with enhanced sensitivity at 1550 nm," *Applied Physics Letters*, vol. 86, no. 24, Article ID 241103, 3 pages, 2005.
- [11] H. Chen, X. Luo, and A. W. Poon, "Cavity-enhanced photocurrent generation by 1.55 μm wavelengths linear absorption in a p-i-n diode embedded silicon microring resonator," *Applied Physics Letters*, vol. 95, no. 17, Article ID 171111, 2009.
- [12] S. Zhu, M. B. Yu, G. Q. Lo, and D. L. Kwong, "Near-infrared waveguide-based nickel silicide Schottky-barrier photodetector for optical communications," *Applied Physics Letters*, vol. 92, no. 8, Article ID 081103, 2008.
- [13] A. Akbari and P. Berini, "Schottky contact surface-plasmon detector integrated with an asymmetric metal stripe waveguide," *Applied Physics Letters*, vol. 95, no. 2, Article ID 021104, 2009.
- [14] Y. Wang, X. Su, Y. Zhu et al., "Photocurrent in Ag-Si photodiodes modulated by plasmonic nanopatterns," *Applied Physics Letters*, vol. 95, no. 24, Article ID 241106, 2009.
- [15] W. F. Kosonocky, F. V. Shallcross, T. S. Villani, and J. V. Groppe, "160 \times 244 element PtSi Schottky-barrier IR-CCD image sensor," *IEEE Transactions on Electron Devices*, vol. 32, no. 8, pp. 1564–1573, 1986.
- [16] R. H. Fowler, "The analysis of photoelectric sensitivity curves for clean metals at various temperatures," *Physical Review*, vol. 38, no. 1, pp. 45–56, 1931.
- [17] V. E. Vickers, "Model of Schottky barrier hot-electron-mode photodetection," *Applied Optics*, vol. 10, no. 9, pp. 2190–2192, 1971.
- [18] S. M. Sze, *Physics of Semiconductor Devices*, John Wiley & Sons, New York, NY, USA, 1981.
- [19] H. X. Yuan and A. G. U. Perera, "Dark current analysis of Si homojunction interfacial work function internal photoemission far-infrared detectors," *Applied Physics Letters*, vol. 66, no. 17, pp. 2262–2264, 1995.
- [20] M. K. Emsley, O. Dosunmu, and M. S. Ünlü, "Silicon substrates with buried distributed Bragg reflectors for resonant cavity-enhanced optoelectronics," *IEEE Journal on Selected Topics in Quantum Electronics*, vol. 8, no. 4, pp. 948–955, 2002.
- [21] E. Y. Chan and H. C. Card, "Near IR interband transitions and optical parameters of metal-germanium contacts," *Applied Optics*, vol. 19, no. 8, pp. 1309–1315, 1980.
- [22] G. G. Shahidi, "SOI technology for the GHz era," *IBM Journal of Research and Development*, vol. 46, no. 2-3, pp. 121–131, 2002.
- [23] E. Y. Chan, H. C. Card, and M. C. Teich, "Internal photoemission mechanisms at interfaces between germanium and thin metal films," *IEEE Journal of Quantum Electronics*, vol. 16, no. 3, pp. 373–381, 1980.
- [24] P. Yeh, *Optical Waves in Layered Media*, John Wiley & Sons, New York, NY, USA, 1988.

- [25] M. A. Muriel and A. Carballar, "Internal field distributions in fiber Bragg gratings," *IEEE Photonics Technology Letters*, vol. 9, no. 7, pp. 955–960, 1997.
- [26] K. Kishino, M. S. Unlu, J. Chyi, J. Reed, L. Arsenault, and H. Morkoc, "Resonant cavity-enhanced (RCE) photodetectors," *IEEE Journal of Quantum Electronics*, vol. 27, no. 8, pp. 2025–2034, 1991.
- [27] E. D. Palik, *Handbook of Optical Constants of Solids*, Academic Press, San Diego, Calif, USA, 1985.
- [28] H. C. Card, "Aluminum-silicon Schottky barriers and ohmic contacts in integrated circuits," *IEEE Transactions on Electron Devices*, vol. 23, no. 6, pp. 538–544, 1976.
- [29] K. Vedam, "Spectroscopic ellipsometry: a historical overview," *Thin Solid Films*, vol. 313–314, pp. 1–9, 1998.
- [30] G. E. Jellison Jr., "The calculation of thin film parameters from spectroscopic ellipsometry data," *Thin Solid Films*, vol. 290–291, pp. 40–45, 1996.
- [31] G. E. Jellison Jr. and F. A. Modine, "Parameterization of the optical functions of amorphous materials in the interband region," *Applied Physics Letters*, vol. 69, no. 3, pp. 371–373, 1996.
- [32] G. E. Jellison Jr., F. A. Modine, P. Doshi, and A. Rohatgi, "Spectroscopic ellipsometry characterization of thin-film silicon nitride," *Thin Solid Films*, vol. 313–314, pp. 193–197, 1998.
- [33] P. Doshi, G. E. Jellison Jr., and A. Rohatgi, "Characterization and optimization of absorbing plasma-enhanced chemical vapor deposited antireflection coatings for silicon photovoltaics," *Applied Optics*, vol. 36, no. 30, pp. 7826–7837, 1997.
- [34] D. E. Aspnes, J. B. Theeten, and F. Hottier, "Investigation of effective-medium models of microscopic surface roughness by spectroscopic ellipsometry," *Physical Review B*, vol. 20, no. 8, pp. 3292–3302, 1979.
- [35] S. Donati, *Photodetectors: Devices, Circuits, and Applications*, Prentice Hall PTR, Upper Saddle River, NJ, USA, 1999.
- [36] W. Demtroder, *Laser Spectroscopy: Vol. 1: Basic principles*, chapter 4, Springer, Berlin, Germany, 2008.

